# Proposal on How to Model the Unloading in a Compaction Equation of State based upon Tri-axial tests on Dry Sand

Leo Laine[a,*] and Ola Pramm Larsen[b]

[a]ANKER – ZEMER Engineering AS
Stugvägen 4, SE-438 94 HÄRRYDA, Sweden
[*]Corresponding author: leo.laine@telia.com

[b]ANKER – ZEMER Engineering AS
P.O. Box 253, NO-0702 OSLO, Norway

This paper proposes how a compaction Equation of State (EOS) can be used to describe the unloading wave as a function of both density and pressure. The modification will result in a more accurate way to calculate the shock wave propagation and attenuation in dry sand. Previously, only an elastic unloading was available in the compaction EOS in AUTODYN by specifying the elastic bulk sound speed as a function of density. Currently, a nonlinear modification is available which relates the slope to a user defined bulk module as a function of density. However, neither of these options captures properly the nonlinear behaviour seen in tri-axial test data during unloading and how the unloading curve shape varies with both density and pressure.

The proposed modifications to the unloading phase for the compaction EOS are based upon tri-axial isotropic and shear tests performed on dry sand. The elastic pressure and shear wave velocities were also measured during isotropic loading. Isotropic unloading was performed from different pressure levels. The results show how the proposed modification which considers both density and pressure for calculating the slope of the unloading can represent the tri-axial test data within the measured pressure range and up to the theoretical maximum density.

## INTRODUCTION

The Swedish Civil Contingencies Agency (MSB) is responsible for the building regulations of the Swedish civil defence shelters. There are specific rules for how the defence shelters are planned, built, equipped and maintained [1]. One of many regulations state what loading level the shelters should withstand: "The effect of a pressure wave corresponding to that produced by a 250 kg GP-bomb with 50 weight per cent TNT which burst freely outside at a distance of 5.0 meters from the outside of the shelter during free pressure release". However, many of the shelters are designed as basements below ground surface. This is the reason why more knowledge on how the ground shock propagates and attenuates during the scaled distances of 0.1 to 10 kg/m$^3$ and affects buried shelters, is needed.

During the Second World War extensive experiment series and research were conducted on ground shock generated by high explosives [2]. This early work functions as a foundation for understanding the behaviour of how the shock waves propagates and attenuates in earth media. In [2], Lampson states that the pressure in the soil from the detonation of an explosive charge is propagated by a plastic wave which is characterized by a continuous change of shape and of duration with distance from the charge, see Fig. 1 for illustration. Close to the source the shape will be sharp and after a distance it will start to attenuate and change shape of the wave.
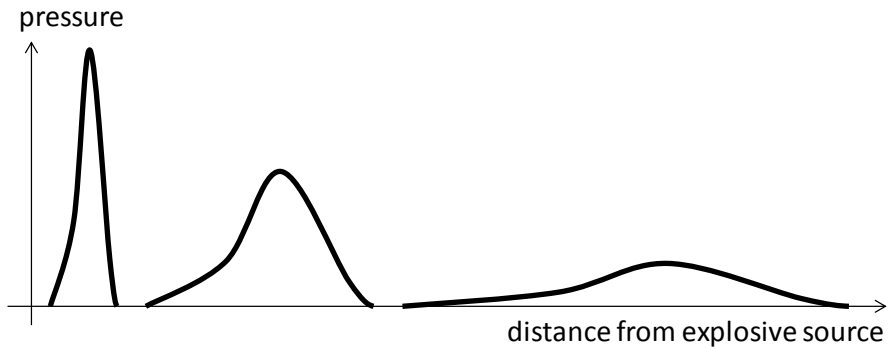
Fig. 1. Illustration of how the ground shock wave change shape during propagation in a compactable soil.

As already stated in [2] by Lampson, the reason for the continuous change of shape is the pressure density relationship which is common for compactable soils, see Fig. 2. The left illustration in Fig.2 shows the loading and unloading path for a generic compactable soil. This curve also defines the loading and unloading wave speed at a certain pressure and density, see right illustration in Fig. 2. The relationship between pressure, density and wave speed $c$ is simply seen as

$$c = \sqrt{\frac{\partial P}{\partial \rho}}. \tag{1}$$

The right illustration Fig.2 shows that the unloading wave speed is higher than the loading wave speed when above a certain pressure level. This means that the high pressure shape will attenuate fast by the unloading. For lower pressures the unloading speed can be slower which would result in that the wave shape starts to have a long unloading tail.
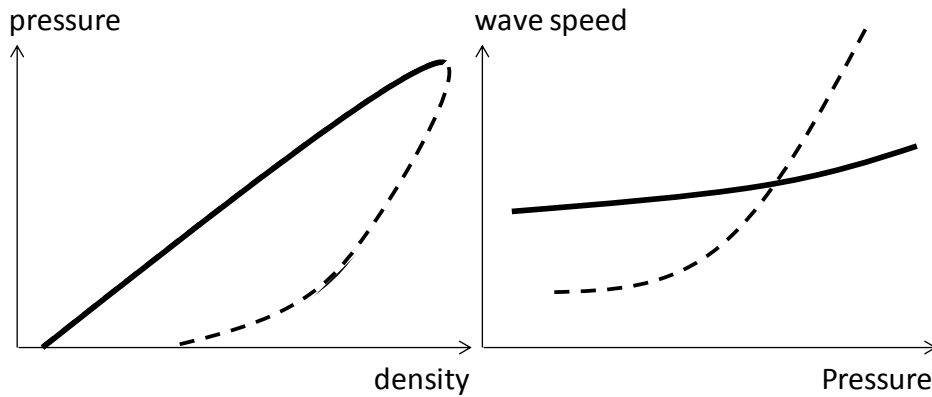


Fig. 2. Illustration of a compactable soil and how the pressure density curve relates to wave speeds as a function of pressure. Solid and dashed lines represent loading and unloading, respectively.

A simple way of modelling compaction materials is to define the plastic compaction curve as a pressure function of density $P(\rho)$ and the unloading wave speed as a function of density $c(\rho)$, see Fig. 3 for illustration. The unloading is then represented by the straight lines on top of the dashed unloading curves, in Fig. 3. Earlier work by Laine et al. on deriving mechanical properties for dry sand from tri-axial experiments, [3] [4], have been widely used for shock simulation involving dry sand within the AUTODYN community [5] with quite descent results e.g. for determining the blast load from buried mines, see e.g. [6] [7]. Here the linear approximation of the unloading curves does not influence the results except for determining the level of shock wave energy absorbed by the dry sand. It is correctly stated in [8] that the material data provided for dry sand in Laine et al. [3] does not include an easy change on how moisture affects the input parameters of the compaction EOS. The original compaction model [10] would need a

totally new set of input when the soil type changes in water contents, porosity, and soil skeleton. In [11] a total of 16 generic soil types were generated from dry sand to fully saturated clay. However, the main deficiency of the original model [10] and the given data for dry sand [3] for the compaction EOS is that the unloading phase is too simplified to properly model the shock wave propagation and the change in shape of the pressure wave as stated in [1]. One way to solve this is to try model the soil as a three phase medium shown in [12] which is a quite interesting approach. However, in this paper a different approach is introduced. The same experimental data for dry sand as shown in [3] and [4] are re-visited to derive how the unloading wave speed can be defined as a function of both density and pressure i.e. $c(\rho,P)$ for the dry sand. The proposed modelling of the unloading phase improves on the model previously presented and previously derived material data for the dry sand with respect to describing how the ground shock pressure wave propagation and change in shape varies with distance from detonation and time.

The proposed modelling captures the dashed unloading curves, as illustrated in Fig.3 for the whole density and pressure domain as well as the transition into fully compacted material. The fully compacted state is reached at ($\rho_n$, $P_n$). At this point the material is seen as linear material with Theoretical Maximum Density (TMD) $\rho_{TMD}$ at zero pressure, see Fig. 3.
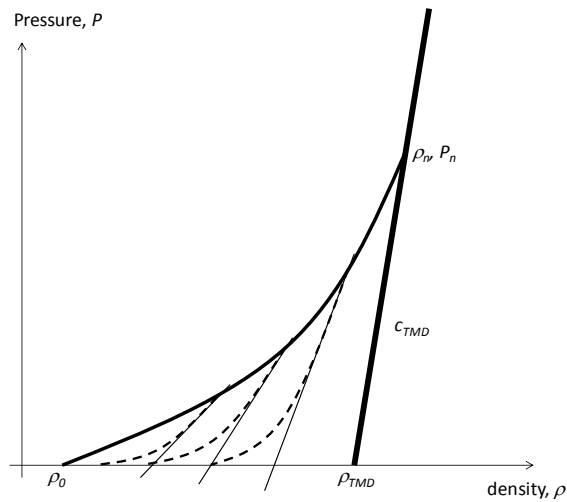


Fig. 3. Illustration of an EOS compaction, where the solid line between ($\rho_0$, $P_0=0$) and ($\rho_n$, $P_n$) shows a plastic compaction curve, dashed lines illustrate nonlinear unloading and the straight lines on top of the dashed lines show linear approximation with elastic unloading wave $c(\rho)$. The point ($\rho_n$, $P_n$) defines when the material is seen as fully compacted and has a linear elastic wave speed of $c_{TMD}$.

The paper is organized as follows: The section EXPERIMENTAL RESULTS AND EARLIER PROPOSED SAND MODELLING will re-visit the experimental results with focus on the compaction EOS and the unloading. Further information on the shear strength; see [3] and [11]. In the section DERIVATION OF HOW THE UNLOADING WAVE SPEED IS A FUNCTION OF BOTH DENSITY AND PRESSURE the optimization formulation and the logical steps are shown for the defining the surface $c(\rho,P)$ from the experimental results. In the section COMPARISON OF UNLOADING PROPERTIES BETWEEN OLD AND NEW EOS the initial unloading wave speed and specific energy properties are compared. Finally the section CONCLUSIONS AND FUTURE WORK sums up the proposed model and provides suggestions for future work.


## EXPERIMENTAL RESULTS AND EARLIER PROPOSED SAND MODELLING

The Norwegian Geotechnical Institute ("NGI") has characterised the soil and performed tri-axial tests on the sand from Sjöbo Sweden [4], see also [3]. The characterization of the soil showed that the grain size distribution in the sand was medium to coarse, with grain size number C60/C10 approximately equal to two. The content of organic compounds was less than one percent. The in situ dry density was approximately 1574 kg/m$^3$; the average water content was approximately 6.57 percent. Finally, the average specific weight of the grains was 2641 kg/m$^3$.

For the experimental setup, two types of tri-axial cell devices were used for the seven tests performed. Firstly, the "NGI standard Cell device" [3] was used for tests up to 2 000 kPa in confinement stress, and secondly for tests above this confinement stress a rock tri-axial cell device was used, see Fig. 4. A cylindrical soil specimen with $h$=90 mm and $d$=38 mm in the rock tri-axial cell was enclosed in a rubber membrane inside the cell. By using a fluid in the chamber, the confining stress (pressure) equal to $\sigma_r=\sigma_2=\sigma_3$ was applied. The vertical stress $\sigma_v=\sigma_1$ was applied by a steel piston, which was employed by hydraulic pumps and a step motor. Additionally the rock tri-axial cell was equipped with pressure transducers to allow measurements of the elastic shear and longitudinal wave speeds of the soil specimen during different pressure and density states.
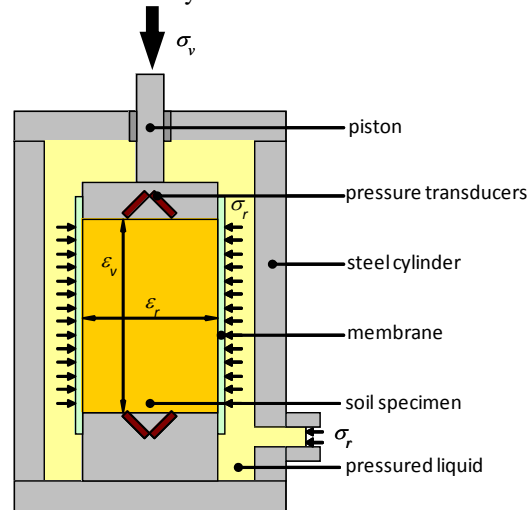


Fig. 4. The rock tri-axial cell device was used for the dry sand with maximum isotropic consolidation pressure of 60 000 kPa [4].

The loading onto the specimen was first an isotropic consolidation ($P=\sigma_v=\sigma_r$) with loading and unloading to different pressure levels, see Fig. 5 - Fig. 7. Radial meter gauges were used to measure radial strain. From this part of the test, the compaction EOS with plastic loading and the mechanical unloading at different pressures levels can be derived. After the isotropic consolidation, a shear test at different pressure levels, i.e. 2 000, 20 000, and 60 000 [kPa] were performed. The radial stresses were kept constant (i.e. $\sigma_r$ = constant) while the vertical stress $\sigma_v$ was increased. Consequently, the maximum yield surface was established from the tests, see further in [3] and [4].
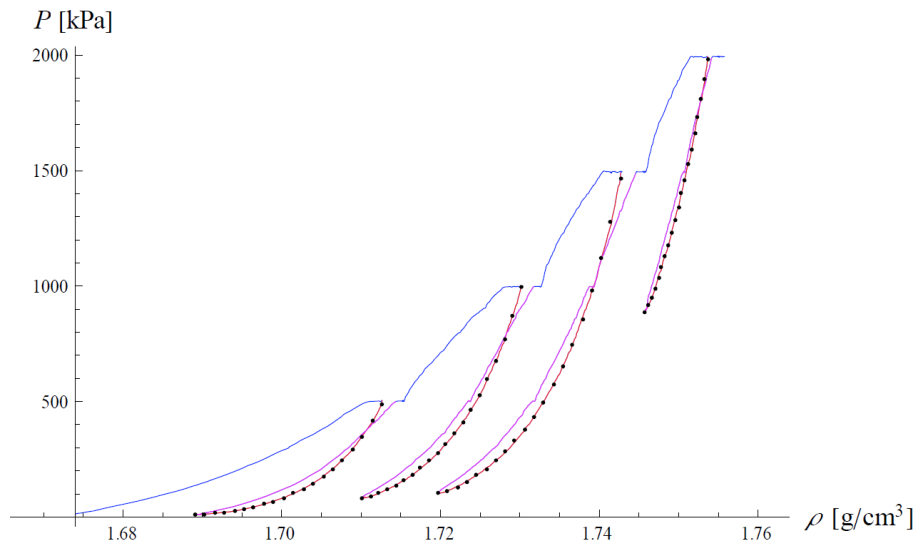


Fig. 5. Experimental data, Test 6, pressure as a function of density, with isotropic consolidation pressure up to 2 000 kPa. The black dots are used as a simplified representation of the unloading curves.
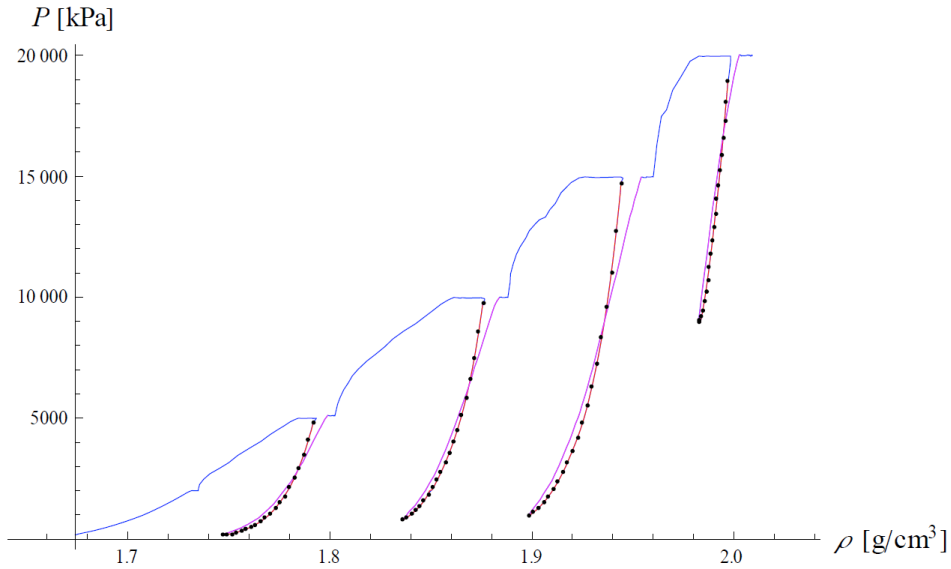
Fig. 6. Experimental data, Tri845, pressure as a function of density, with isotropic consolidation pressure up to 20 000 kPa. The black dots are used as a simplified representation of the unloading curves.
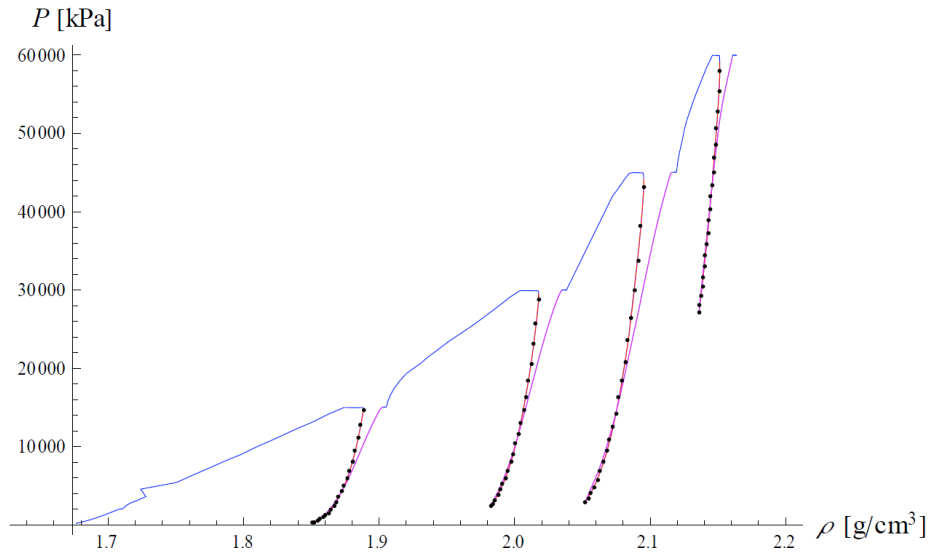


Fig. 7. Experimental data, Tri847, pressure as a function of density, with isotropic consolidation pressure up to 60 000 kPa. The black dots are used as a simplified representation of the unloading curves.

Measurements of elastic longitudinal $v_l$ and shear $v_s$ wave speeds were performed by using the pressure transducers, shown in Fig. 3, for certain density and pressure levels. However, the measurements of the elastic waves were mainly performed when the pressure was not close to zero. In Fig. 8 the derived bulk sound speed $c$ from the original material data for the dry sand is shown. The bulk sound speed $c$ is based upon following relationship

$$c = \sqrt{v_l^2 - \frac{4}{3} v_s^2}.$$ (2)

In addition, a linear extrapolation was used for $c$ for densities above 2150 kg/m$^3$. The theoretical maximum density was set equal to the grain density of $\rho_{TMD}$=2641 kg/m$^3$. The maximum bulk sound speed was set equal to $c_{TMD}$=4636 m/s based upon shock Hugoniot data found for westerly granite [3].
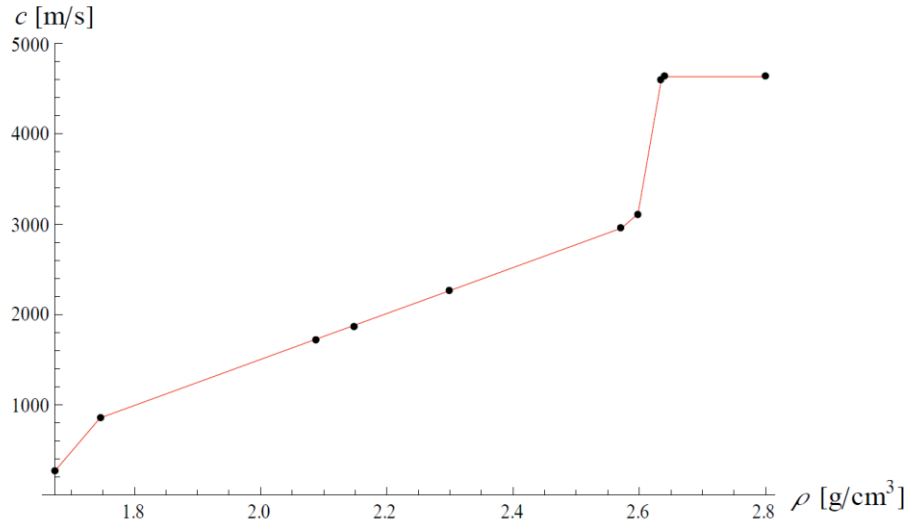


Fig. 8. Experimentally derived bulk sound speed as a function of density $c_b(\rho)$.

Fig. 8 illustrates the deficiency in the current material model when defining different unloading wave speeds based on density alone, and not including pressure which is an essential part when properly describing the change in shape of the propagating pressure wave

## DERIVATION OF HOW THE UNLOADING WAVE SPEED IS A FUNCTION OF BOTH DENSITY AND PRESSURE

Used symbols and parameters when deriving the shape of the unloading wave speed as a function of density and pressure are given in Table 1.

Table 1. Used symbols and explanations.

| Symbol | Explanation |
|---|---|
| $\lambda$ | Intersection of arbitrary unloading curve with the $P$=0 line. |
| $P_c(\rho)$ | Plastic compaction curve. One of the primary inputs to the old EOS, a piecewise linear curve using 10 user defined data points in AUTODYN. |
| $P_U(\rho)$ | Functional expression for an arbitrary unloading curve |
| $\rho_L(\lambda)$ | Density span of unloading curve from $\rho=\lambda$ at the $P$=0 line to the intersection point with $P_c(\rho)$ at $\rho=\rho_{int}$. $\rho_L(\lambda) = \rho_{int} - \lambda$ |
| $\rho_0$ | Initial or in situ density of the soil including water content. |
| $\rho_{TMD}$ | Theoretical maximum density. |
| $\rho_{int}$ | Density value at intersection point between the plastic compaction curve and an arbitrary unloading curve. |
| $\rho_{crit}$ | User input controlling the exponential growth of the $c(\rho,P=0)$ curve. $\rho<\rho_{crit}$ results in unloading wave speeds less than $c_0$ at $P$=0. |
| $c(\rho,P)$ | Unloading wave speed, not the same as speed of sound, see eq. (1). |
| $c_b(\rho)$ | Bulk speed of sound as a function of density. One of the primary inputs to the old EOS, a piecewise linear curve using 10 user defined data points in AUTODYN. |
| $c_0$ | Initial sound speed at initial density $\rho=\rho_0$. |
| $c_{TMD}$ | Sound speed when theoretical maximum density is reached. At this level of maximum compression the EOS is perfectly linear elastic, meaning that the unloading wave speed is identical to the bulk speed of sound. |
| $c_{min}$ | User input for the minimal unloading wave speed at $\rho=\rho_0$, $P$=0. |

The cornerstone of the new compaction EOS is a complete description of the unloading wave speed $c(\rho,P)$ for the complete state space $(\rho,P)$ of the granular material. The state space can easily be visualized by the area confined by the plastic compaction curve, $P=0$ line, and the fully elastic unloading/loading path as shown in Fig. 3. When the unloading wave speed surface $c(\rho,P)$ is obtained every unloading/loading path is unambiguously defined through the relation:

$$\frac{\partial P_U(\rho)}{\partial \rho} = c(\rho,P)^2 \tag{3}$$

With the initial condition $P_i = P_U(\rho_i)$. The $(\rho_i,P_i)$ is an arbitrary material state in the state space domain. Also note that the loading path will be identical to the unloading path for this new compaction EOS.

Assuming that only a handful of experimental unloading data sets are available, which was the case for the unloading/loading data employed in this derivation, it is necessary to make rigorous use of the boundary values, i.e. $P_c(\rho)$ and $c_b(\rho)$, and various extrapolation techniques. The objective is to derive the general trend of the unloading patterns exhibited by the experimental data while at the same time satisfying the theoretical boundary values.

Here follows an overview of the basic **steps** involved in the derivation of the $c(\rho,P)$ surface.

**Step 1:** A lot of effort was put into the search of a general functional expression $P_U(\rho)$ that could fit the various experimental unloading patterns, satisfy the underlying physics, and at the same time involve a relative simple mathematical construct. Based on numerous curve fitting attempts of many different functional expressions on the experimental data, polynomials of different orders, logarithms, splines, exponentials and combinations of these were systematically tested for applicability. Finally, a best candidate was finally chosen

$$P_U(\rho) = \left(d + e^a\left(e^{b(\rho-\lambda)} - 1\right)\right)(\rho - \lambda) \tag{4}$$

$$\frac{\partial P_U(\rho)}{\partial \rho} = d + e^a\left(e^{b(\rho-\lambda)} - 1\right) + be^{a+b(\rho-\lambda)}(\rho - \lambda) \tag{5}$$

$$\frac{\partial P_U{}^n(\rho)}{\partial \rho^n} = nb^{(n-1)}e^{a+b(\rho-\lambda)} + b^n e^{a+b(\rho-\lambda)}(\rho - \lambda), n \geq 2 \tag{6}$$

where $a$, $b$, $d$, and $\lambda$ are constant parameters that will be determined based on various curve fitting techniques. Eq. (4) is the primary function, Eq. (5) is the unloading slope, and Eq. (6) is the nth derivative.

$P_U(\rho)$ has following convenient properties:

1. $P_U(\lambda) = 0$.
2. $\delta P_U(\lambda)/\delta \rho = d$, which makes it easy to determine slope at $P=0$.
3. $P_U(\rho)$ and all its derivatives are continuously growing functions for $\rho > \lambda$ assuming $d>0$ and $b>0$.
4. $P_U(\rho)$ has a relative simple functional description, and is numerically robust.

**Step 2:** In order to extract the global unloading behaviour, certain dominating trends were extracted based on observations from the local curve fitting level. I.e. the experimental data from each unloading sequence was curve fitted based on the $P_U(\rho)$ functional description, and properties like the intersection with the $P_c(\rho)$ curve and the $P=0$ line were determined with $\rho=\rho_{int}$ and $\rho=\lambda$ respectively, see Fig. 9. Another important extrapolated property of the unloading curve was the slope $\frac{\partial P_U(\lambda)}{\partial \rho}$ at $P=0$, see Fig. 9.
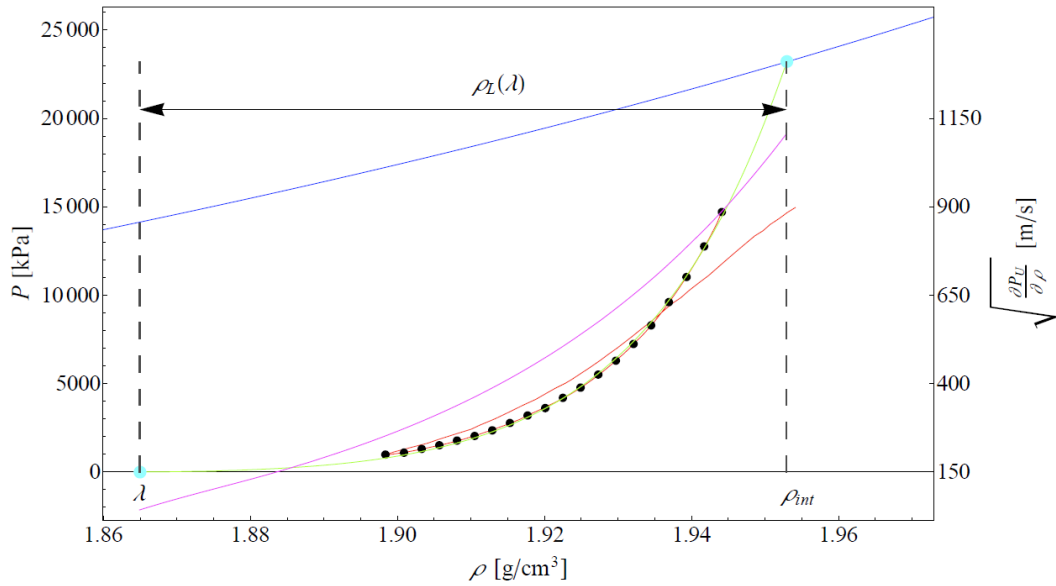
Fig. 9. Optimization results of fitting the $P_U(\rho)$ function through the unloading experimental data represented by black dots. Blue curve shows plastic compaction as a function of density, green curve a numerical fit of the $P_U(\rho)$ function through the experimental unloading data. Magenta curve is the square root of the slope to the $P_U(\rho)$ function. The scale on the right side of the plot applies to the magenta curve only.

The global unloading properties were described by using two mathematical constructs shown in Fig. 10 and Fig. 11. Fig. 10 describes the unloading wave speed $c(\rho,P=0)$ at zero pressure. Fig. 11 describes the density span $\rho_L(\lambda)$ for the unloading curves. $c(\rho,P=0)$ was rigidly applied, while $\rho_L(\lambda)$ was only used as a guidance for the optimization process, which lead to the creation of extrapolated unloading curves outside the experimental data domain.
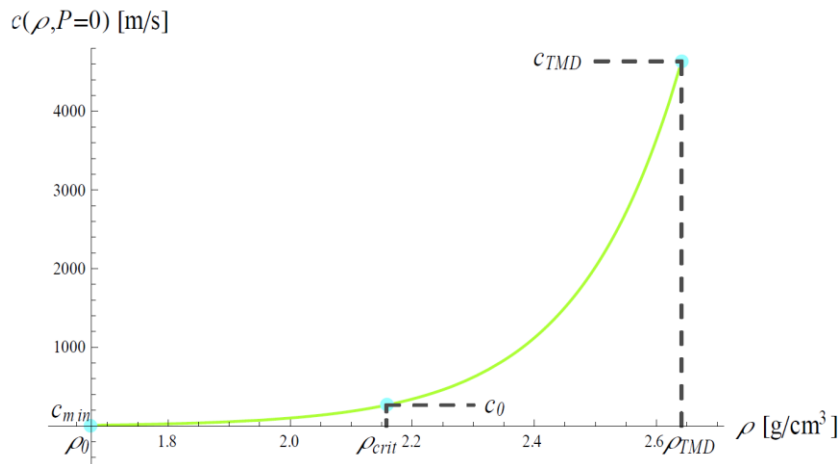


Fig. 10. Green curve illustrates how the transition from minimum unloading wave speed transforms to theoretical maximum density unloading wave speed at $P=0$.
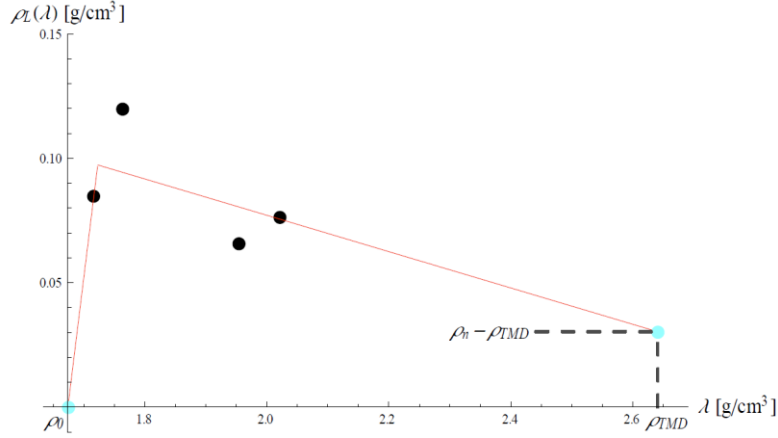
Fig. 11. General descriptions of the density span which provides a guideline to the extrapolation of unloading curves outside the experimental data domain. The black dots represent the density span $\rho_{L,i}$ for a selection of the experimental unloading data. The red line is the fitted bilinear $\rho_L(\lambda)$ curve satisfying the boundary values at $\rho_0$ and $\rho_{TMD}$.

**Step 3:** The extrapolated $c(\lambda_i, P=0)$ values for each unloading curve (i) produces the basis for constructing the exponential $c(\rho, P=0)$ curve in Fig. 10. A lower bound $c_{min}$, a theoretical upper bound $c_{TMD}$, and a critical $c_{crit}$ value could alternatively be specified to uniquely determine the exponential $c(\rho, P=0)$ curve if there are limited experimental data points near the $P=0$ line.

**Step 4:** By using the $c(\rho, P=0)$ curve and the $\rho_L(\lambda)$ guideline together with the plastic compaction curve and the bulk sound speed curve, one can numerically approximate each unloading curve by using Non-Linear-Programming (NLP). For an arbitrary unloading curve starting at the $P=0$ line at $\rho=\lambda_k$ the NLP problem reads as follows

$$\min_{a,b,d,\rho_{int}} (\lambda_k + \rho_L(\lambda_k) - \rho_{int})^2 \tag{7}$$

subject to

$$\frac{\partial P_U(\lambda_k)}{\partial \rho} = d = c(\lambda_k, P=0)^2 \tag{8}$$

$$P_U(\rho_{int}) = P_c(\rho_{int}) \tag{9}$$

$$\frac{\partial P_U(\rho_{int})}{\partial \rho} = c_b(\rho_{int})^2 \tag{10}$$

$$\rho_0 < \lambda_k < \rho_{TMD} \tag{11}$$

$$\rho_0 < \lambda_k < \rho_{int} < \rho_n \tag{12}$$

$$b > 0 \tag{13}$$

where Eq. 7 is minimizing the deviation to the to the $\rho_L$ density span guidance. The minimization is subject to constraints such as Eq. 8 which constrains the slope at $P=0$ to the global trend, see Fig. 10. The Eq. 9 constrains the $\rho_{int}$ to be the intersection of $P_U$ and $P_c$. The Eq. 10 constrains the slope to the bulk sound speed at $\rho_{int}$. Eq. 11 and Eq. 12 constrains the valid density domain for the starting point and ending point of the unloading curve, respectively. Finally, Eq. 13 maintain the convenient properties of the $P_U(\rho)$ function. In Table 2 a selection of results are summarized from the optimization.

Table 2. A selection of experimentally fitted, red in Fig. 12, and extrapolated, magenta in Fig. 12, unloading curves with their corresponding parameter values providing the exponential unloading curves $P_U(\rho)$. The pressure value $P$ provides the pressure level on the plastic compaction curve where the unloading is initialized. The extrapolated unloading curves are generated through the NLP optimization procedure outlined in Eq.7 - Eq.13.

| Pressure $P$ [kPa] | Experimental or NLP Extrapolated Unloading curve | P=0 intersection $\lambda$ [g/cm$^3$] | $P_c(\rho)$ intersection $\rho_{int}$ [g/cm$^3$] | $P_U(\rho)$ const. $a$ Log[m$^2$/s$^2$] | $P_U(\rho)$ const. $b$ [cm$^3$/g] | $P_U(\rho)$ const. $d$ [m$^2$/s$^2$] |
|---|---|---|---|---|---|---|
| 3200 | NLP | 1.689 | 1.719 | 12.20 | 26.45 | 131.3 |
| 9000 | Experimental | 1.717 | 1.801 | 7.002 | 54.24 | 210.1 |
| 15800 | Experimental | 1.791 | 1.884 | 7.785 | 45.91 | 660.5 |
| 23100 | Experimental | 1.865 | 1.953 | 8.928 | 40.62 | 1829 |
| 32500 | Experimental | 1.938 | 2.020 | 8.978 | 47.89 | 4715 |
| 47400 | Experimental | 2.021 | 2.097 | 10.67 | 35.79 | 13410 |
| 62000 | Experimental | 2.082 | 2.153 | 11.82 | 27.61 | 28230 |
| 78600 | NLP | 2.136 | 2.203 | 12.40 | 25.65 | 54320 |
| 99500 | NLP | 2.190 | 2.253 | 13.08 | 22.22 | 104000 |
| 136000 | NLP | 2.262 | 2.320 | 14.40 | 13.34 | 245700 |
| 188000 | NLP | 2.334 | 2.390 | 19.02 | 0.2759 | 578100 |
| 269000 | NLP | 2.407 | 2.469 | 21.15 | 3.082e-2 | 1.356e6 |
| 376600 | NLP | 2.479 | 2.544 | 21.79 | 1.347e-2 | 3.177e6 |
| 508000 | NLP | 2.569 | 2.613 | 25.44 | 4.691e-4 | 9.189e6 |

**Step 5:** A finite set of unloading curves then provide the basis for generating a Non-Uniform-Rational-B-Spline (NURBS) surface ultimately resulting in the definition of $c(\rho,P)$, see Fig. 12, Fig. 13, and Fig. 14 for different views. Red curves in Fig. 12 represent locally curve fitted experimental unloading data, while the magenta curves are extrapolated through the NLP problem described over. The solid green curve is the $c(\rho,P=0)$ curve while the green wall behind the blue/pink NURBS surface represent the plastic compaction and bulk sound speed, i.e. $P_c(\rho)$, and $c_b(\rho)$. The significance of the green wall can be better understood if the surface is projected in the $(\rho,P)$ plane Fig. 13, and the $(\rho,c)$ plane Fig. 14. In Fig. 14 the projected curve that travels along the top of the green wall and then merges with the NURBS surface (blue/pink) is actually the bulk sound speed $c_b(\rho)$. Notice that the unloading wave speed realized by the experimentally fitted red curves end up at a level approximately 10-20% under the bulk sound speed curve.

It is important to note that the NURBS surface will only function as an intermediary when considering the planned implementation into AUTODYN. The NURBS surface will later on be broken down into a set of piecewise polynomial surfaces to provide faster numerical evaluation of the $c(\rho,P)$ function.
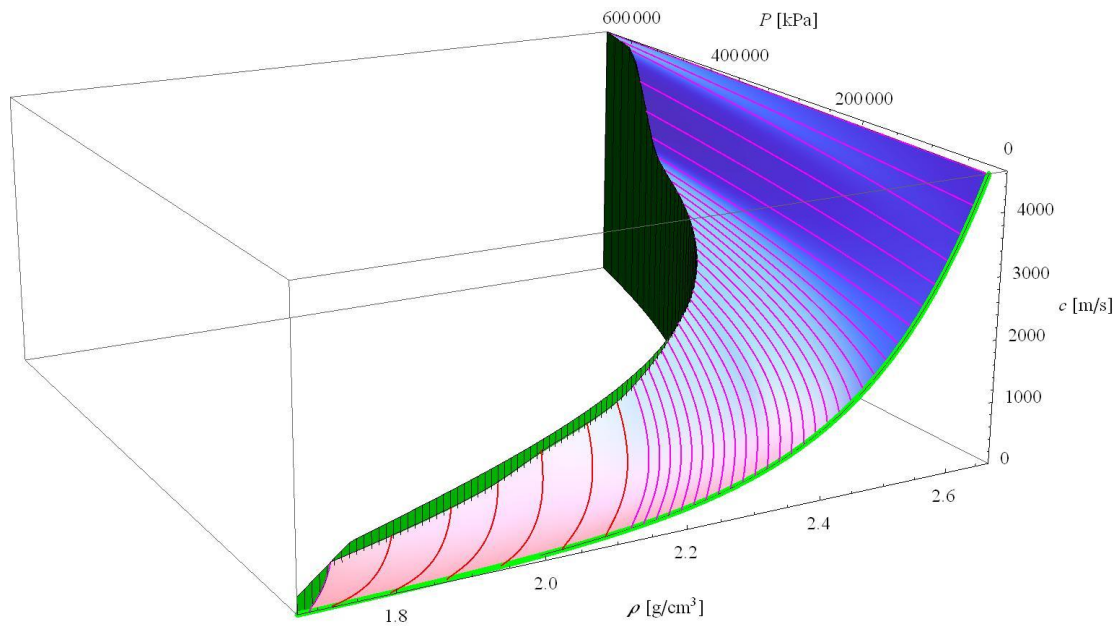
Fig. 12. 3D surface in blue to pink colours of unloading wave speed as a function of both pressure and density, $c(\rho,P)$.
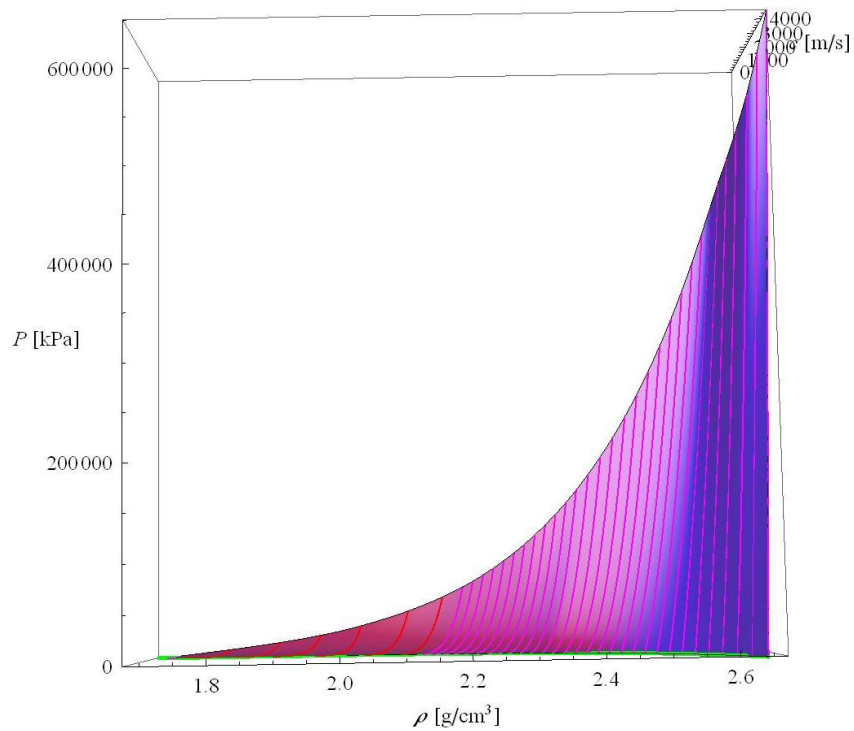


Fig. 13. 3D surface of unloading wave speed as a function of both pressure and density from a density versus pressure view. The projected curve is the plastic compaction curve $P_{\mathrm{c}}(\rho)$
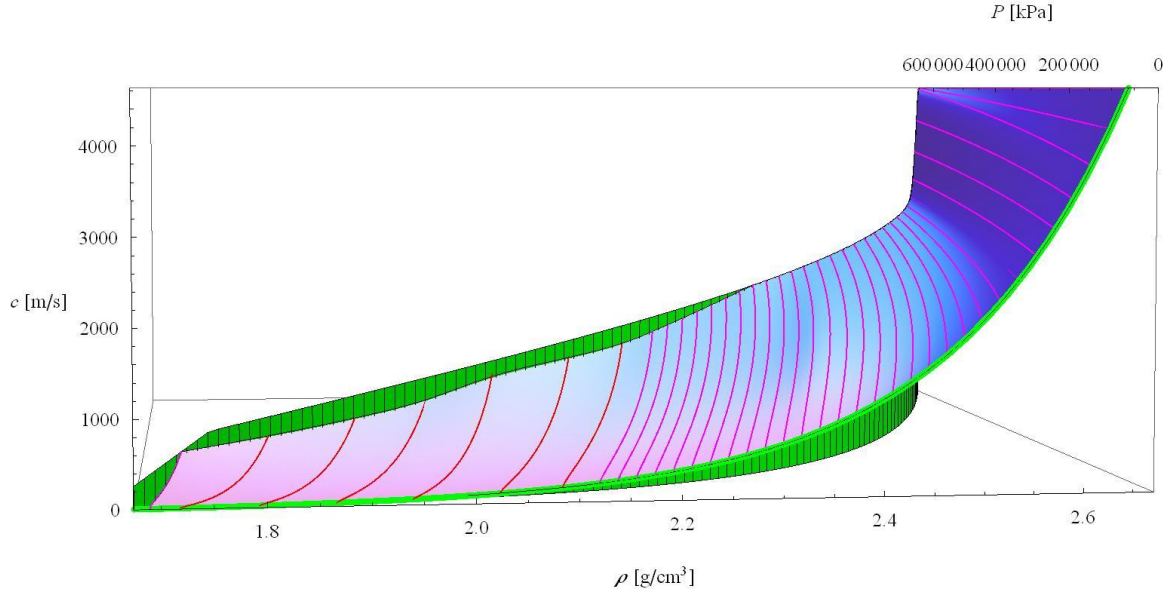
Fig. 14. 3D surface of unloading wave speed as a function of both pressure and density from a density versus wave speed view.


## COMPARISON OF UNLOADING PROPERTIES BETWEEN OLD AND NEW EOS

Two interesting properties of the unloading phase in the new and old EOS are here compared: the initial unloading wave speed when starting the unloading phase and the specific energy. Firstly, the measured bulk sound speed $c_b$, see Fig. 8, is compared with the derived initial unloading wave speed from using the measured isotropic tri-axial tests, see Fig.5-Fig.7. The summary in Table 3 shows that the difference is in the 10-20% range for initial wave speed by using the two different approaches. The difference in initial unloading wave speed is considered as a minor issue because the unloading will be better represented in its entirety with the new proposal.

Table 3. Comparison of initial unloading wave speeds with old and new EOS.

| Pressure $P$ [kPa] | old EOS $c$ [m/s] | new EOS $c$ [m/s] | Decrease from old to new EOS [%] |
|---|---|---|---|
| 9000 | 994 | 775 | 22 |
| 15800 | 1200 | 980 | 18.9 |
| 23100 | 1380 | 1160 | 15.9 |
| 32500 | 1550 | 1440 | 7.2 |
| 47400 | 1750 | 1630 | 6.5 |
| 62000 | 1890 | 1730 | 8.5 |

The second point in comparing the absorbed specific energy between unloading with old and new EOS is shown in Fig. 15. The unloading is calculated accordingly

$$e = \int_{\rho_1}^{\rho_2} \frac{P(\rho)}{\rho^2} d\rho \qquad\qquad (14)$$

Table 4 compares the specific unloading and total specific energy absorbed. Interesting to note is the specific unloading energy is almost 199 percent higher at 9 000 kPa in starting unloading pressure for the new EOS. The total specific energy absorbed at 3 200 and 9 000 kPa in starting unloading pressure results in 8 and 16 percent decrease in total specific energy absorbed for the new EOS. For higher unloading pressures as e.g. 225 000 kPa the reduction is only 2 percent which indicates that the old model works quite well for high pressure simulations such as buried tank mine simulations where the focus is only on how much energy the covering dry sand absorbed from the burst and confinement. The actual unloading curve shapes are shown in Fig. 15.
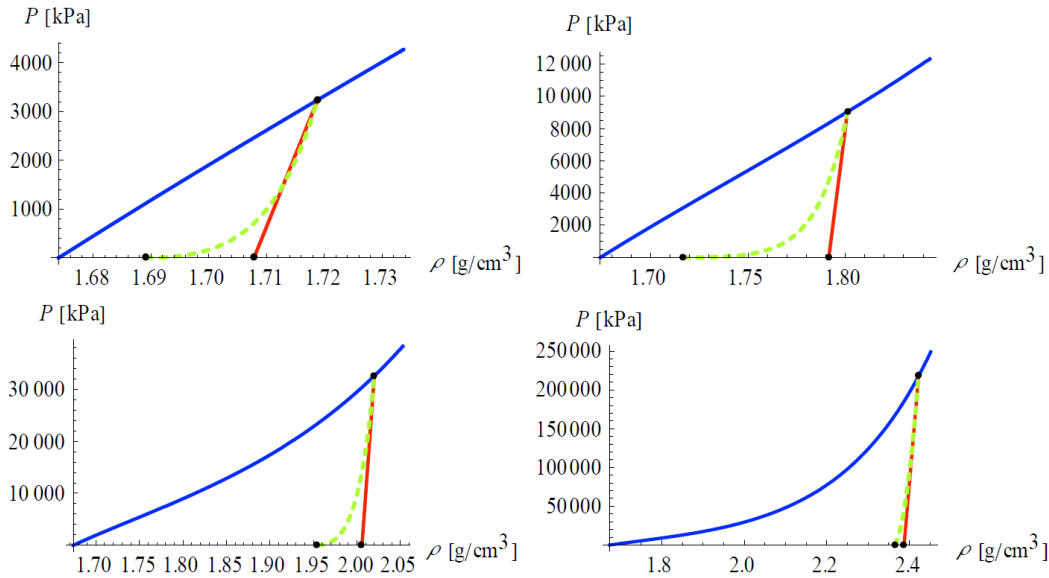
Fig. 15 illustrates unloading curves starting at different unloading pressures. The solid red line and dashed green line represent the unloading by the old EOS and the new EOS, respectively. From upper left, upper right, lower left, and lower right, 3 200, 9 000, 32 500, and 225 000 kPa, as starting unloading pressure, respectively.

Table 4. Comparison of difference in specific unloading and total specific energy absorbed between old EOS and new EOS.

| Load case | | Specific unloading energy old EOS | Specific unloading energy new EOS | Increase from old to new EOS | | Total specific energy absorbed by old EOS | Total specific energy absorbed by new EOS | Decrease from old to new EOS |
|---|---|---|---|---|---|---|---|---|
| [kPa] | | [J/kg] | [J/kg] | [%] | | [J/kg] | [J/kg] | [%] |
| 3200 | | 6.0 | 7.7 | 27 | | 19 | 18 | 8 |
| 9000 | | 13 | 40 | 199 | | 173 | 146 | 16 |
| 32500 | | 57 | 125 | 120 | | 1260 | 1190 | 5 |
| 225000 | | 693 | 852 | 23 | | 8570 | 8410 | 2 |

## CONCLUSIONS AND FUTURE WORK

A 3D representation of how the unloading wave speed $c(\rho,P)$ is both density and pressure dependent was here derived for the dry sand from Sjöbo Sweden, see Fig. 16. It shows how the unloading wave speed changes with different regions. The ridge is the part that is similar to what was used as input in the old model. I.e. the unloading wave speed is only a function of density $c(\rho)$. Now when the pressure part is added, i.e. $c(\rho,P)$, the unloading wave speed nicely curves down when the pressure approaches zero. A minimum unloading wave speed at pressure equal to zero is illustrated by the green curve.

For future work it is an open question how the implementation into AUTODYN is made most robust for user input variations. If good quality is assured from isotropic tri-axial loading experiments it is proposed that the input for the modified EOS could be unloading curves like shown in Fig.5-Fig.7 in addition to the plastic compaction curve, initial density $\rho_0$, theoretical maximum density $\rho_{TMD}$, and theoretical maximum density elastic unloading wave speed $c_{TMD}$. When it comes to fit the Granular Strength model it is important to properly represent the elastic shear waves

which means that the shear modulus $G$ has to be mapped for the whole $c(\rho,P)$ domain. This will be a part of future work.
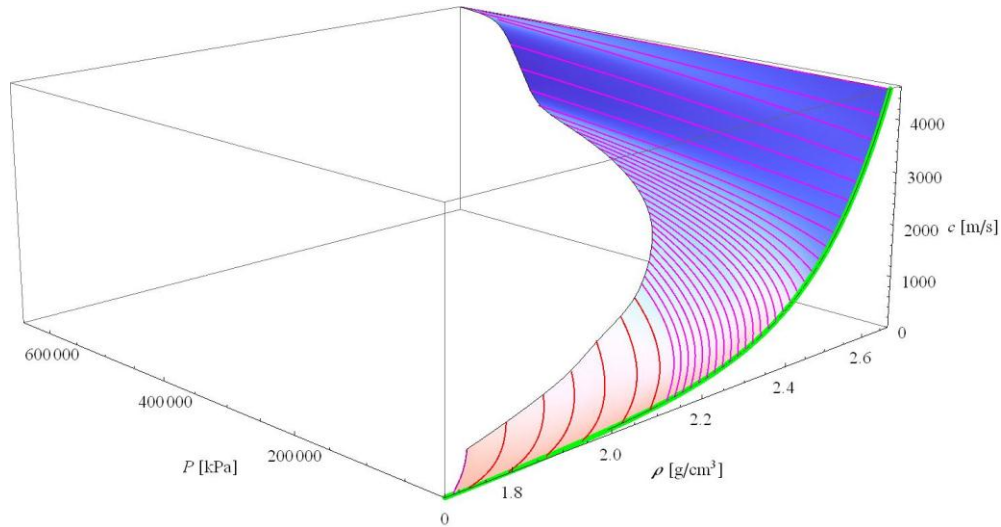


Fig. 16. NURBS surface of the derived unloading wave speed $c(\rho,P)$ from dry Sjöbo sand Sweden. Red curves represent experimentally fitted unloading data, while the magenta curves are extrapolated curves from the NLP solution.

## ACKNOWLEDGEMENTS

## REFERENCES

[1] Ekengren B. (2009): *Skyddsrum, SR 09 (Civil Defence Shelters SR 09, in Swedish.)*, the Swedish Civil Contingencies Agency (MSB), B54-141/09, Karlstad, Sweden.

[2] Lampson C.W. (1946): Final Report on Effects of Underground Explosions, Div. 2, National Defence Research Committee of the US Office Scientific R&D, NDRC Report No. A-479, OSRD Report No. 6645.

[3] Laine L. and Sandvik A. (2001): "Derivation of mechanical properties for sand", *4th Asian-Pacific conference on Shock and Impact Loads on Structures*, CI-Premier PTE LTD, vol. 4,  pp 353-360, Singapore.

[4] Heyerdahl H. and Madshus C. (2000): "EOS-data for sand, Tri-axial tests on sand from Sjöbo", Norges Geotekniske institutt, NGI rept. 20001157-1, Oslo, Norway.

[5] Century Dynamics Inc., (2004): *AUTODYN Theory Manual Revision 5.0*, San Ramon, CA, USA.

[6] Fairlie G. and Bergeron D. (2002):"Numerical simulations of Mine Blast Loading on Structures", *17th Numerical aspects of Blast Symposium*, Las Vegas, Nevada.

[7] Tjernberg A. (2006): *Simulation of Mine-Blast deflection*, FOI-Swedish Defence Research Agency, Technical Report, FOI-R--1913--SE, TUMBA, Sweden.

[8] Grujicic M., Pandurangan B., Qiao R., Cheeseman B.A., Roy W.N., Skaggs R.R., and Gupta R. (2008): Parameterization of the porous-material model for sand with different levels of water saturation", Soil Dynamics and Earthquake Engineering 28, pp 20–35

[10] Moxnes J. F., Ødegårdstuen G., Atwood A., and Curran P. (1999): "Mechanical properties of a porous material studied in a high speed piston driven compaction experiment", 30th International Annual Conference of ICT Energetic Materials, Fraunhofer Institut Chemische Technologie.

[11] Laine L. (2006): "Study of Planar Ground Shock in Different Soils and Its Propagation Around a Rigid Block", *77th Shock and Vibration Symposium*, Monterey, CA.

[12] Wang1 Z., Hao H., and Lu Y. (2004): "A three-phase soil model for simulating stress wave propagation due to blast loading", *Int. Journal for Numerical and Analytical Methods in Geomechanics,* 28:33–56 (DOI: 10.1002/nag.325).